Natural convection along a micro-patterned vertical wall. Part 1: A multiscale homogenization approach to establish *effective* boundary conditions

Essam Nabil Ahmed[a,*], Alessandro Bottaro[a], Giovanni Tanda[b]

[a]*DICCA, Università degli Studi di Genova, via Montallegro 1, 16145 Genova, Italy*
[b]*DIME, Università degli Studi di Genova, via Montallegro 1, 16145, Genova, Italy*

Abstract

Asymptotic homogenization is employed to formulate upscaled *effective* boundary conditions at a smooth virtual surface for a natural convection flow over a periodically-roughened vertical surface, to bypass the expensive numerical resolution of flow and temperature fields near and within the wall corrugations. Microscale problems are found by expanding near-wall variables in terms of a small parameter ϵ, ratio between the microscopic and the macroscopic length scales. The expressions of the upscaled velocity and temperature boundary conditions are provided up to second-order accuracy in ϵ. As a typical implementation of the theory, the case of transverse square ribs is considered. The classical Navier-slip condition for the streamwise and the spanwise velocity components is modified at second order by the gradient of the normal stress and the time-derivative of the shear stress. The streamwise slip velocity is additionally corrected by a buoyancy term at first order and a temperature gradient term at second order. The normal velocity at the virtual surface appears only as a second-order transpiration condition. A Robin-like condition for the temperature is found, where the wall temperature is corrected with a temperature gradient term representing thermal slip. The proposed effective conditions provide insight into the physical complexity of the interaction between microscopic

---

*Corresponding author
Email address: essameldin.abdo@edu.unige.it (Essam Nabil Ahmed)

and macroscopic domains when heat transfer is present in the motion of a fluid along a rough surface, and quantify the role of the buoyancy force within the microscopic layer on the macro-behavior of the flow, previously unaccounted for.

1. Introduction and literature review

In the present work, the multiscale homogenization approach is proposed to simplify the numerical simulations of buoyancy-driven flows over periodically-roughened vertical surfaces, while maintaining an acceptable level of accuracy.

5　Asymptotic homogenization is an approach which targets the study of the macroscale behavior of a medium which contains microscopic details, by replacing the rapidly varying properties related to the heterogeneity of the medium, associated with surface irregularities, porous structures, different phases, etc., by equivalent homogeneous macroscopic properties [1]. This technique can play

10　a pivotal role when handling differential equations that govern physical problems with microscale fluctuations [2] which are characterized by some sort of periodicity or pseudo-periodicity. These problems can be computationally simplified by first solving ad hoc auxiliary systems of equations in a microscopic domain to evaluate the necessary *upscaled* conditions by means of averaging.

15　The approach relies on the asymptotic expansion of the dependent variables in terms of a wisely-chosen small parameter whose existence is related to the presence of well-separated scales, for instance a microscopic length scale (ℓ) and a macroscopic length scale $(L >> \ell)$ so that the parameter $\epsilon = \frac{\ell}{L} << 1$ can be defined, and the solution of the problem can be sought up to different orders of

20　accuracy in terms of ϵ.

Multiscale homogenization has been known and used by applied mathematicians for a long time. Nonetheless, its practical relevance had not been imme-

2

diately noticed by engineers and physicists. In recent years, homogenization
²⁵ has been re-discovered and applied to a variety of relevant cases. Flow over
micro-textured surfaces represents a typical homogenization problem. Jiménez
and Vernescu [3] have derived the Navier-slip effective condition for the Stokes
flow over a rough surface via homogenization theory as a first-order corrector
term to the no-slip condition of a smooth surface. Zampogna et al. [4] have
³⁰ pursued a generalization of the classical first-order Navier-slip condition [5] over
a rough surface by means of a third-order Navier-slip tensor. The homogenized
model was pushed to second-order by Lācis et al. [6] with the introduction of a
transpiration velocity, the normal velocity component at the fictitious interface,
thus enhancing model predictions for a turbulent boundary layer over a rough
³⁵ surface. A further improvement has been added by Bottaro and Naqvi [7] who
sought a solution up to third-order accuracy. For earlier studies along the same
lines, the reader is referred to [8, 9, 10]. The range of applications subtended by
homogenization theory is being continuously widened and enhancements to the
basic formulation are ongoing. Zampogna et al. [11] have extended the theory
⁴⁰ to the study of the turbulent flow over compliant riblets, seeking reduction of
the skin friction drag. Effective boundary conditions at the interface between a
porous bed and an unconfined flow region have been explored by Sudhakar et al.
[12] and Naqvi and Bottaro [13]. *Adjoint* homogenization has been introduced
by Bottaro [14] as a method to take into account non-linear effects within the
⁴⁵ microscopic region.

The buoyancy-driven flow over periodically roughened vertical surfaces is an
ideal application of the asymptotic homogenization approach, through which
the macroscopic behavior of the free convective flows can be predicted at a
⁵⁰ reduced computational cost and a significant level of accuracy, to replace time-
consuming feature-resolving simulations. So far, the full capturing of surface
details has been the standard way to carry out numerical work [15, 16, 17, 18],
and this implies that the implementation of multiscale homogenization for nat-
ural convection studies is a fertile field which deserves to be well defined and

3

₅₅ efficiently employed.

The work presented in this paper is a novel implementation of the multiscale homogenization technique to study natural convection heat transfer over rough surfaces. The only previous contribution in this aspect was the work by Introïni ₆₀ et al. [19] who applied the volume-averaging upscaling method to the study of the steady laminar buoyancy-driven flow over rough surfaces. However, their model suffered from some deficiencies that limit its applicability range. A critical assumption adopted by Introïni was the neglect of buoyancy effects within the microscopic region, so that momentum and energy conservation equations ₆₅ are decoupled. This assumption, despite being mathematically advantageous, limits the model applicability to cases in which the Rayleigh number characterizing the microscopic problem (based on the microscopic length scale and the temperature difference across the microscopic region) is sufficiently small. To satisfy this condition, the bulk Rayleigh number must be lower than some ₇₀ threshold value and the roughness elements must be confined within the thermal boundary layer. In practical situations, high values of the Rayleigh number are often encountered. Moreover, being first-order accurate, the method developed by Introïni et al. [19] has some restrictions on the utilization of the approach. To assess the validity of their model, Introïni and co-workers carried out differ- ₇₅ ent numerical simulations on a differentially heated stamp-shaped cavity. The results showed that the validity of the model is not guaranteed for values of the bulk Rayleigh number higher than 10^7.

In this paper asymptotic homogenization is used to formulate expressions ₈₀ for the macroscopic velocity and temperature effective conditions at a virtual interface separating the microscopic and the macroscopic sub-domains. The Boussinesq hypothesis is employed so that the buoyancy term that appears in the microscopic momentum equation is linearly coupled with the energy equation; this represents a substantial difference with the work by Introïni et al. [19]. ₈₅ The dependent parameters are expanded asymptotically in powers of the small

4

parameter $\epsilon = \frac{pattern\ periodicity\ (\ell)}{plate\ length\ (L)}$. The effective conditions for velocity and temperature are all sought up to second-order accuracy. In the next section, the governing equations and the boundary conditions of the problem are outlined, the representative scales are chosen, and the continuity condition at the matching surface is discussed. In Sect. 3, the microscopic region is considered where the asymptotic expansion of the dependent variables is defined, and the problem is reconstructed at different orders of ϵ. For each order, generic forms of the solutions are assumed and *auxiliary* differential systems are formulated. Then, the case of transverse square ribs is discussed in Sect. 4. The parameters of interest are determined, via numerical solution of the auxiliary systems, and the effect of the matching surface location is considered. For convenience, the results are extrapolated to the fictitious surface going through the outer rim of the ribs. A parametric study seeking the effect of varying the rib size to the pitch distance ratio on the different coefficients is presented in Sect. 5. In the concluding section, the effects of the defined parameters are highlighted.

12 warnings

2. Governing equations and domain decomposition

2.1. The dimensional equations

As a major assumption, the changes in the density of the fluid are considered to only affect the buoyancy term in the momentum conservation equation. Under the Boussinesq approximation, the conservation equations in terms of the dimensional variables, space coordinates $\hat{x}_i$, time $\hat{t}$, pressure $\hat{P}$, velocity $\hat{u}_i$, and temperature $\hat{T}$, are expressed as follows:

$$\frac{\partial \hat{u}_i}{\partial \hat{x}_i} = 0, \tag{1-a}$$

$$\hat{\rho}_\infty \left(\frac{\partial \hat{u}_i}{\partial \hat{t}} + \hat{u}_j \frac{\partial \hat{u}_i}{\partial \hat{x}_j} \right) = -\frac{\partial(\hat{P} - \hat{P}_\infty)}{\partial \hat{x}_i} + \mu \frac{\partial^2 \hat{u}_i}{\partial \hat{x}_j^2} - \hat{\rho}_\infty \beta (\hat{T} - \hat{T}_\infty) g_i, \tag{1-b}$$

$$\frac{\partial \hat{T}}{\partial \hat{t}} + \hat{u}_j \frac{\partial \hat{T}}{\partial \hat{x}_j} = \alpha \frac{\partial^2 \hat{T}}{\partial \hat{x}_j^2}, \tag{1-c}$$

with $\hat{\rho}_\infty$, $\hat{P}_\infty$ and $\hat{T}_\infty$ the density, pressure and temperature in the stagnant flow region, sufficiently far away from the vertical wall. The parameters assumed constant in the equations above are the volumetric thermal expansion coefficient, β, the dynamic viscosity, $\mu = \hat{\rho}_\infty \nu$, with ν the kinematic viscosity, and the thermal diffusivity, α. With the axes as in Figure 1, the volume force per unit mass has components $g_i = -g\, \delta_{i1}$ with g the acceleration of gravity and δ_{ij} the Kronecker index. The parameter controlling the thermal convection flow is the Rayleigh number Ra, defined as

$$Ra = \frac{g\beta(\hat{T}_w - \hat{T}_\infty)L^3}{\alpha\nu},$$

where the temperature of the wall, $\hat{T}_w$, is maintained constant, and the plate length, L, is the macroscopic length scale of the problem. We also define the Grashof number, $Gr = Ra/Pr$, with $Pr = \nu/\alpha$ the Prandtl number, a property

6

of the fluid. Given the presence of two characteristic length scales, a macroscopic and a microscopic one, the latter related to the periodicity l of the microstructures present on the vertical surface, two problems will be set up. These two problems will be coupled at some distance from the wall, a distance that is asymptotically large when seen from the microscopic point of view and asymptotically small when seen from the macroscopic viewpoint.
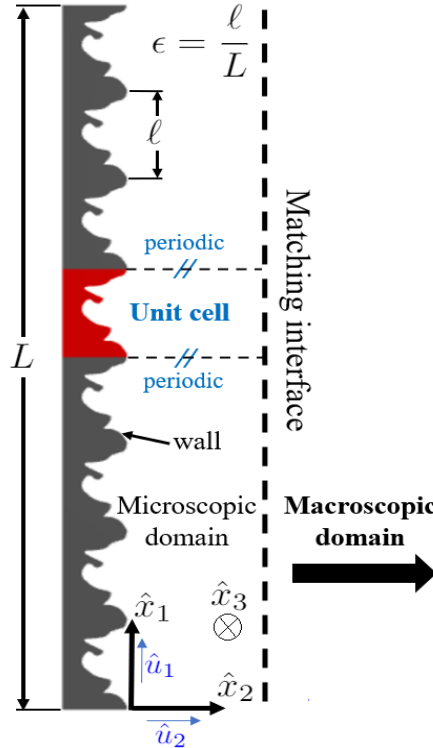
Figure 1: Sketch of a general vertical rough surface, periodically micro-patterned, with notations and indication of microscopic and macroscopic domains.

2.2. The macroscale problem

To set the proper scales of the macroscopic problem we consider the fact that the motion of the fluid is generated by the buoyancy force; if $\mathcal{U}$ is the characteristic velocity of the fluid, we can write

$$\frac{\hat{\rho}_\infty \mathcal{U}^2}{L} \sim \hat{\rho}_\infty \beta (\hat{T}_w - \hat{T}_\infty) g.$$

7

We thus define the velocity scale $\mathcal{U} = \sqrt{\beta(\hat{T}_w - \hat{T}_\infty)gL} = Gr^{1/2}\dfrac{\nu}{L}$ and normalize the velocity vector as:

$$U_i = \frac{\hat{u}_i}{\mathcal{U}}.$$

The other dimensionless variables are defined as follows:

$$X_i = \frac{\hat{x}_i}{L}, \quad t = \frac{\hat{t}\mathcal{U}}{L}, \quad P = \frac{\hat{P} - \hat{P}_\infty}{\hat{\rho}_\infty \mathcal{U}^2}, \quad \Theta = \frac{\hat{T} - \hat{T}_\infty}{\hat{T}_w - \hat{T}_\infty},$$

for the balance equations to become:

$$\frac{\partial U_i}{\partial X_i} = 0, \tag{2-a}$$

$$\frac{\partial U_i}{\partial t} + U_j \frac{\partial U_i}{\partial X_j} = -\frac{\partial P}{\partial X_i} + \frac{1}{\sqrt{Gr}} \frac{\partial^2 U_i}{\partial X_j^2} + \Theta \delta_{i1}, \tag{2-b}$$

$$Pr\sqrt{Gr}\left(\frac{\partial \Theta}{\partial t} + U_j \frac{\partial \Theta}{\partial X_j}\right) = \frac{\partial^2 \Theta}{\partial X_j^2}. \tag{2-c}$$

These equations depend on only the macroscopic independent variables, t and X_i, and must be solved subject to matching conditions at $X_2 \to 0$, together with $\Theta = U_i = 0$ for $X_2 \to \infty$.

2.3. The microscale problem

The near-wall problem differs from the previous one in that the microscopic velocity scale is taken to be $\epsilon\mathcal{U}$, with $\epsilon = \frac{pattern\ periodicity\ (\ell)}{plate\ length\ (L)} \ll 1$. Also, the pressure scale for the near-wall flow is the viscous pressure, i.e. $\mu\left(\epsilon\mathcal{U}\right)/l$. Dimensionless variables in the microscopic domain are introduced as follows:

$$u_i = \frac{\hat{u}_i}{\epsilon\mathcal{U}}, \quad x_i = \frac{\hat{x}_i}{l}, \quad t = \frac{\hat{t}\mathcal{U}}{L}, \quad p = \frac{(\hat{P} - \hat{P}_\infty)L}{\mu\mathcal{U}}, \quad \theta = \frac{\hat{T} - \hat{T}_\infty}{\hat{T}_w - \hat{T}_\infty}.$$

The microscopic dimensionless equations are:

$$\frac{\partial u_i}{\partial x_i} = 0, \tag{3-a}$$

$$\epsilon\mathcal{R}_G\left(\frac{\partial u_i}{\partial t} + u_j \frac{\partial u_i}{\partial x_j}\right) = -\frac{\partial p}{\partial x_i} + \frac{\partial^2 u_i}{\partial x_j^2} + \mathcal{R}_G\,\theta\,\delta_{i1}, \tag{3-b}$$

8

$$\epsilon \mathcal{R}_G \, Pr \left(\frac{\partial \theta}{\partial t} + u_j \frac{\partial \theta}{\partial x_j} \right) = \frac{\partial^2 \theta}{\partial x_j^2}, \qquad \text{(3-c)}$$

with the reduced Grashof number R_G, defined by $R_G = \epsilon \sqrt{Gr}$, assumed of order one. The microscale problem is bounded by the microstructured wall on one side; therefore, the following condition is imposed at this location.

$$u_i = 0, \quad \theta = 1 \quad \text{for} \;\; y = y_w, \qquad \text{(3-d)}$$

with $y_w = y_w \, (x_1, x_3)$ the micro-patterned wall. A *representative volume element* must be chosen, of unit length along x_1 and x_3 (cf. Figure 1), and periodic conditions are enforced for all dependent variables along these directions. On account of the scalings adopted for inner (i.e., near-wall) and outer problems, the conditions for $x_2 \to \infty$ are:

$$-p \, \delta_{i2} + \left(\frac{\partial u_i}{\partial x_2} + \frac{\partial u_2}{\partial x_i} \right) = S^{i2}, \qquad \text{(3-e)}$$

$$\frac{\partial \theta}{\partial x_2} = \epsilon \, \eta; \qquad \text{(3-f)}$$

these amount to matching the components of the traction vector and of the heat flux between the two regions. For ease of notation in the equations above we have introduced the following definitions for the macroscopic dimensionless stresses in the streamwise, normal, and spanwise directions (respectively S^{12}, S^{22}, S^{32}) as well as the macroscopic dimensionless normal temperature gradient (η):

$$S^{i2} = -Gr^{1/2} \, P \, \delta_{i2} + \left(\frac{\partial U_i}{\partial X_2} + \frac{\partial U_2}{\partial X_i} \right),$$

$$\eta = \frac{\partial \Theta}{\partial X_2}.$$

Notice that both S^{i2} and η depend on only macroscopic variables; they represent the forcing of the outer flow on the near-wall state.

We still need to specify the asymptotic matching conditions which will eventually result in *effective boundary conditions* for the macroscopic problem, to

be applied some distance from the microstructured wall. They are:

$$\lim_{X_2 \to 0} U_i = \lim_{x_2 \to \infty} \epsilon \, u_i, \qquad \lim_{X_2 \to 0} \Theta = \lim_{x_2 \to \infty} \theta. \tag{4-a, b}$$

3. Asymptotic analysis of the microscale problem

3.1. Expansion of the inner variables

Asymptotic expansions in terms of the small parameter ϵ are introduced, and like-order terms are collected, leading to a hierarchy of problems. We impose:

$$u_i = u_i^{(0)} + \epsilon \, u_i^{(1)} + \epsilon^2 \, u_i^{(2)} + ...,$$

and likewise for p and θ. Furthermore, using the chain rule we replace in the microscopic equations the term $\dfrac{\partial}{\partial x_i}$ by $\dfrac{\partial}{\partial x_i} + \epsilon \, \dfrac{\partial}{\partial X_i}$. The asymptotic expressions are plugged into Eqs. (3) governing the microscale problem.

3.2. Reconstruction of the problem at different orders

The problems at the asymptotic orders of interest are given below.

3.2.1. $\mathcal{O}(\epsilon^0)$ problem

$$\frac{\partial u_i^{(0)}}{\partial x_i} = 0, \tag{5-a}$$

$$-\frac{\partial p^{(0)}}{\partial x_i} + \frac{\partial^2 u_i^{(0)}}{\partial x_j^2} + \mathcal{R}_G \, \theta^{(0)} \, \delta_{i1} = 0, \tag{5-b}$$

$$\frac{\partial^2 \theta^{(0)}}{\partial x_j^2} = 0, \tag{5-c}$$

with boundary conditions

$$u_i^{(0)} = 0, \quad \theta^{(0)} = 1 \quad \text{at} \ \ x_2 = y_w, \tag{5-d}$$

$$-p^{(0)} \, \delta_{i2} + \left(\frac{\partial u_i^{(0)}}{\partial x_2} + \frac{\partial u_2^{(0)}}{\partial x_i} \right) = S^{i2}, \quad \frac{\partial \theta^{(0)}}{\partial x_2} = 0 \quad \text{for} \ \ x_2 \to \infty. \tag{5-e}$$

10

A solution of this problem can be sought by separation of variables, on account of the linearity of the system, for the solution to take the form:

$$u_i^{(0)} = \breve{u}_{ik} S^{k2} + u_i^\dagger \mathcal{R}_G, \quad p^{(0)} = \breve{p}_k S^{k2} + p^\dagger \mathcal{R}_G + P_0,$$

with $\breve{u}_{ik}$, $u_i^\dagger$, $\breve{p}_k$, and $p^\dagger$ tensors which depend on microscopic variables only, and

P_0 an integration constant function only of X_j. After plugging the ansatz for the order zero solution into the balance equations, it becomes clear that uniqueness conditions are needed for $\breve{p}_k$ and $p^\dagger$, which appear in the system only through their gradients. We enforce the vanishing of the integrals of $\breve{p}_k$ and $p^\dagger$ over a cubic cell of unit side length positioned sufficiently far from the wall (nominally

for $x_2 \to \infty$); this leads to the vanishing of P_0. It is also clear that we cannot stop the solution at this order, since the leading order temperature solution is simply $\theta^{(0)} = 1$, i.e. the effect of the microstructure appears in the temperature at the next ϵ-order.

The dynamic problem at $\mathcal{O}(\epsilon^0)$ yields the same equations for $\breve{u}_{ik}$ and $\breve{p}_k$ already given for the isothermal case by Bottaro and Naqvi [7], so that we can anticipate that the first correction to the no-slip condition for the velocity will be a Navier-slip term. Such a leading-order problem reads:

$$\frac{\partial \breve{u}_{ik}}{\partial x_i} = 0, \tag{6-a}$$

$$-\frac{\partial \breve{p}_k}{\partial x_i} + \frac{\partial^2 \breve{u}_{ik}}{\partial x_j^2} = 0, \tag{6-b}$$

with

$$\breve{u}_{ik} = 0 \quad \text{at} \quad x_2 = y_w \tag{6-c}$$

$$-\breve{p}_k \, \delta_{i2} + \left(\frac{\partial \breve{u}_{ik}}{\partial x_2} + \frac{\partial \breve{u}_{2k}}{\partial x_i} \right) = \delta_{ik} \quad \text{at} \quad x_2 \to \infty. \tag{6-d}$$

The † variables, which describe the effect of buoyancy on velocity and pressure fields, satisfy the steady system:

$$\frac{\partial u_i^\dagger}{\partial x_i} = 0, \tag{7-a}$$

11

$$-\frac{\partial p^\dagger}{\partial x_i} + \frac{\partial^2 u_i^\dagger}{\partial x_j^2} = -\delta_{i1}, \tag{7-b}$$

with

$$u_i^\dagger = 0 \quad \text{at} \quad x_2 = y_w, \tag{7-c}$$

$$-p^\dagger \delta_{i2} + \left(\frac{\partial u_i^\dagger}{\partial x_2} + \frac{\partial u_2^\dagger}{\partial x_i} \right) = 0 \quad \text{at} \quad x_2 \to \infty. \tag{7-d}$$

As it will be shown later on, the problems can be further simplified when x_3-elongated wall ribs are examined, as in the case of riblets [20, 21].

3.2.2. $\mathcal{O}(\epsilon^1)$ problem

The equations at order ϵ are forced by the order one state, i.e.

$$\frac{\partial u_i^{(1)}}{\partial x_i} = -\frac{\partial u_i^{(0)}}{\partial X_i}, \tag{8-a}$$

$$-\frac{\partial p^{(1)}}{\partial x_i} + \frac{\partial^2 u_i^{(1)}}{\partial x_j^2} + \mathcal{R}_G\, \theta^{(1)}\, \delta_{i1} = \frac{\partial p^{(0)}}{\partial X_i} - 2\frac{\partial^2 u_i^{(0)}}{\partial x_j\, \partial X_j} + \mathcal{R}_G \left(\frac{\partial u_i^{(0)}}{\partial t} + u_j^{(0)} \frac{\partial u_i^{(0)}}{\partial x_j} \right), \tag{8-b}$$

$$\frac{\partial^2 \theta^{(1)}}{\partial x_j^2} = -2\frac{\partial^2 \theta^{(0)}}{\partial x_j\, \partial X_j} + \mathcal{R}_G\, Pr \left(\frac{\partial \theta^{(0)}}{\partial t} + u_j^{(0)} \frac{\partial \theta^{(0)}}{\partial x_j} \right), \tag{8-c}$$

with boundary conditions

$$u_i^{(1)} = \theta^{(1)} = 0 \quad \text{at} \quad x_2 = y_w, \tag{8-d}$$

$$-p^{(1)} \delta_{i2} + \left(\frac{\partial u_i^{(1)}}{\partial x_2} + \frac{\partial u_2^{(1)}}{\partial x_i} \right) = -\left(\frac{\partial u_i^{(0)}}{\partial X_2} + \frac{\partial u_2^{(0)}}{\partial X_i} \right) \quad \text{at} \quad x_2 \to \infty, \tag{8-e}$$

$$\frac{\partial \theta^{(1)}}{\partial x_2} = \eta - \frac{\partial \theta^{(0)}}{\partial X_2} \quad \text{at} \quad x_2 \to \infty. \tag{8-f}$$

12

We must now substitute the results for $u_i^{(0)}$, $p^{(0)}$, and $\theta^{(0)}$ into Eqs. (8-a to 8-f). As a first step, a solution for $\theta^{(1)}$ is to be sought from the energy equation and the corresponding boundary conditions. Specifically, these equations read:

$$\frac{\partial^2 \theta^{(1)}}{\partial x_i^2} = 0, \tag{9-a}$$

$$\theta^{(1)} = 0 \quad \text{at} \quad x_2 = y_w, \tag{9-b}$$

$$\frac{\partial \theta^{(1)}}{\partial x_2} = \eta \quad \text{at} \quad x_2 \to \infty. \tag{9-c}$$

Owing to linearity, the solution can be written as:

$$\theta^{(1)} = \tilde{\theta}(x_i)\ \eta(X_i) \tag{10}$$

The new microscopic field $\tilde{\theta}$ solves the system

$$\frac{\partial^2 \tilde{\theta}}{\partial x_i^2} = 0, \tag{11-a}$$

$$\tilde{\theta} = 0 \quad \text{at} \quad x_2 = y_w, \tag{11-b}$$

$$\frac{\partial \tilde{\theta}}{\partial x_2} = 1 \quad \text{at} \quad x_2 \to \infty. \tag{11-c}$$

The equations governing the behavior of $u_i^{(1)}$ and $p^{(1)}$ can be recast as follows:

$$\frac{\partial u_i^{(1)}}{\partial x_i} = -\breve{u}_{jk}\frac{\partial S^{k2}}{\partial X_j} \tag{12-a}$$

$$-\frac{\partial p^{(1)}}{\partial x_i} + \frac{\partial^2 u_i^{(1)}}{\partial x_j^2} = \mathcal{R}_G^3 u_j^\dagger \frac{\partial u_i^\dagger}{\partial x_j} + \mathcal{R}_G^2 \left[\breve{u}_{jk}\frac{\partial u_i^\dagger}{\partial x_j} + u_j^\dagger \frac{\partial \breve{u}_{ik}}{\partial x_j} \right] S^{k2} \tag{12-b}$$

$$+ \mathcal{R}_G \left[\breve{u}_{jk}\frac{\partial u_{i\ell}}{\partial x_j} \right] S^{k2}S^{\ell 2} + \mathcal{R}_G\,\breve{u}_{ik}\frac{\partial S^{k2}}{\partial t} - \mathcal{R}_G\,\eta\,\tilde{\theta}\,\delta_{i1} + \breve{p}_k\frac{\partial S^{k2}}{\partial X_i} - 2\frac{\partial \breve{u}_{ik}}{\partial x_j}\,\frac{\partial S_{k2}}{\partial X_j},$$

with boundary conditions

$$u_i^{(1)} = 0 \quad \text{at} \quad x_2 = y_w, \tag{12-c}$$

13

$$\frac{\partial u_1^{(1)}}{\partial x_2} + \frac{\partial u_2^{(1)}}{\partial x_1} = -\breve{u}_{1k}\frac{\partial S^{k2}}{\partial X_2} - \breve{u}_{2k}\frac{\partial S^{k2}}{\partial X_1},$$

$$-p^{(1)} + 2\frac{\partial u_2^{(1)}}{\partial x_2} = -2\breve{u}_{2k}\frac{\partial S^{k2}}{\partial X_2}, \tag{12-d}$$

$$\frac{\partial u_3^{(1)}}{\partial x_2} + \frac{\partial u_2^{(1)}}{\partial x_3} = -\breve{u}_{3k}\frac{\partial S^{k2}}{\partial X_2} - \breve{u}_{2k}\frac{\partial S^{k2}}{\partial X_3} \quad \text{at} \quad x_2 \to \infty.$$

Again, a generic form of the solution can sought, i.e.

$$u_i^{(1)} = \dot{u}_{ijk}\left[\frac{\partial S^{k2}}{\partial X_j}\right] + \ddot{u}_{ik}\left[\mathcal{R}_G(S^{k2})^2\right] + \ddot{u}_{i12}\left[\mathcal{R}_G S^{12}S^{22}\right] + \ddot{u}_{i13}\left[\mathcal{R}_G S^{12}S^{32}\right]$$

$$+ \ddot{u}_{i23}\left[\mathcal{R}_G S^{22}S^{32}\right] + u_i{}'\left[\mathcal{R}_G\,\eta\right] + \overline{u}_{ik}\left[\mathcal{R}_G^2 S^{k2}\right] + u_i^{\ddagger}\left[\mathcal{R}_G^3\right] + u_{ik}^t\left[\mathcal{R}_G\frac{\partial S^{k2}}{\partial t}\right], \tag{13-a}$$

$$p^{(1)} = \dot{p}_{jk}\left[\frac{\partial S^{k2}}{\partial X_j}\right] + \ddot{p}_k\left[\mathcal{R}_G(S^{k2})^2\right] + \ddot{p}_{12}\left[\mathcal{R}_G S^{12}S^{22}\right] + \ddot{p}_{13}\left[\mathcal{R}_G S^{12}S^{32}\right]$$

$$+ \ddot{p}_{23}\left[\mathcal{R}_G S^{22}S^{32}\right] + p'\left[\mathcal{R}_G\,\eta\right] + \overline{p}_k\left[\mathcal{R}_G^2 S^{k2}\right] + p^{\ddagger}\left[\mathcal{R}_G^3\right] + p_k^t\left[\mathcal{R}_G\frac{\partial S^{k2}}{\partial t}\right]. \tag{13-b}$$

Twenty-three decoupled systems of equations arise from substituting the preceding forms into Eqs. (12). They are given in Appendix 1.

3.2.3. Taking the temperature condition to higher order

Given that the macroscopic velocity at the matching surface is now available up to order ϵ^2 (cf. Eq. (4-a)), it is advisable to do the same with the temperature. Employing the values of the dependent variables at the earlier orders, the microscopic energy equation at $\mathcal{O}(\epsilon^2)$ now reads

$$\frac{\partial^2\theta^{(2)}}{\partial x_i^2} = Pr\mathcal{R}_G\left[\tilde{\theta}\frac{\partial\eta}{\partial t} + \breve{u}_{jk}\frac{\partial\tilde{\theta}}{\partial x_j}\eta\, S^{k2} + u_j^{\dagger}\frac{\partial\tilde{\theta}}{\partial x_j}\eta\,\mathcal{R}_G\right] - 2\frac{\partial\tilde{\theta}}{\partial x_j}\frac{\partial\eta}{\partial X_j}. \tag{14-a}$$

The boundary conditions are $\theta^{(2)} = 0$ at $x_2 = y_w$ and

$$\frac{\partial\theta^{(2)}}{\partial x_2} = -\tilde{\theta}\frac{\partial\eta}{\partial X_2} \qquad \text{at} \quad x_2 \to \infty. \tag{14-b}$$

The following general form for the solution of $\theta^{(2)}$ may be assumed:

$$\theta^{(2)} = \theta_k^! \left[\frac{\partial \eta}{\partial X_k} \right] + \theta_k^* \left[Pr\mathcal{R}_G \, \eta S^{k2} \right] + \theta^{**} \left[Pr\mathcal{R}_G^2 \, \eta \right] + \theta^t \left[Pr\,\mathcal{R}_G \frac{\partial \eta}{\partial t} \right]. \quad (15)$$

Eight decoupled systems of equations stem from substituting the latter form into Eqs. (14); they are provided in Appendix 2.

4. The case of transverse square ribs

As an example of the implementation of the theory, the case of transverse square ribs is considered so that the auxiliary systems can be significantly simplified. In particular, because of invariance along x_3, all auxiliary problems simplify considerably (with derivatives $\partial/\partial x_3$ set to zero), and only two-dimensional Stokes-like (or Laplace-like, or Poisson-like) problems remain to be solved in the (x_1, x_2) plane, subject to periodic conditions along x_1. A sketch of the microscopic representative volume element is provided in Figure 2.
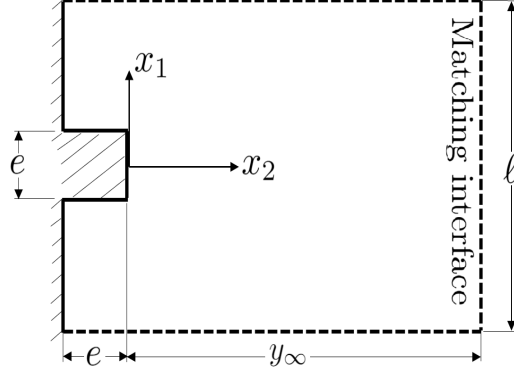
Figure 2: Sketch of a unit cell in the microscopic domain, indicating coordinates and geometric parameters.

Some of the microscopic problems admit trivial solutions. For instance, it is easy to find that in the elementary cell we have $\breve{u}_{12} = \breve{u}_{22} = \breve{u}_{13} = \breve{u}_{23} = \breve{u}_{31} = \breve{u}_{32} = u_3^\dagger = 0$, plus $\breve{p}_2 = -1$ and $\breve{p}_3 = 0$. The systems which do not have a simple solution have been solved numerically by using the STAR-CCM+ multiphysics software (version 15.06.007-R8), by successfully refining the grid until

15

fully grid-converged states are found, for varying dimensions of the cell along x_2. Detailed numerical results of the reduced auxiliary systems relative to the $\mathcal{O}(\epsilon^0)$, $\mathcal{O}(\epsilon^1)$ and $\mathcal{O}(\epsilon^2)$ problems are presented in Appendices 3, 4 and 5, for a rib size to periodicity ratio, e/l, equal to 0.25, and matching interface location positioned at $x_2 = y_\infty = 5$.

4.1. A synthesis of the microscopic results
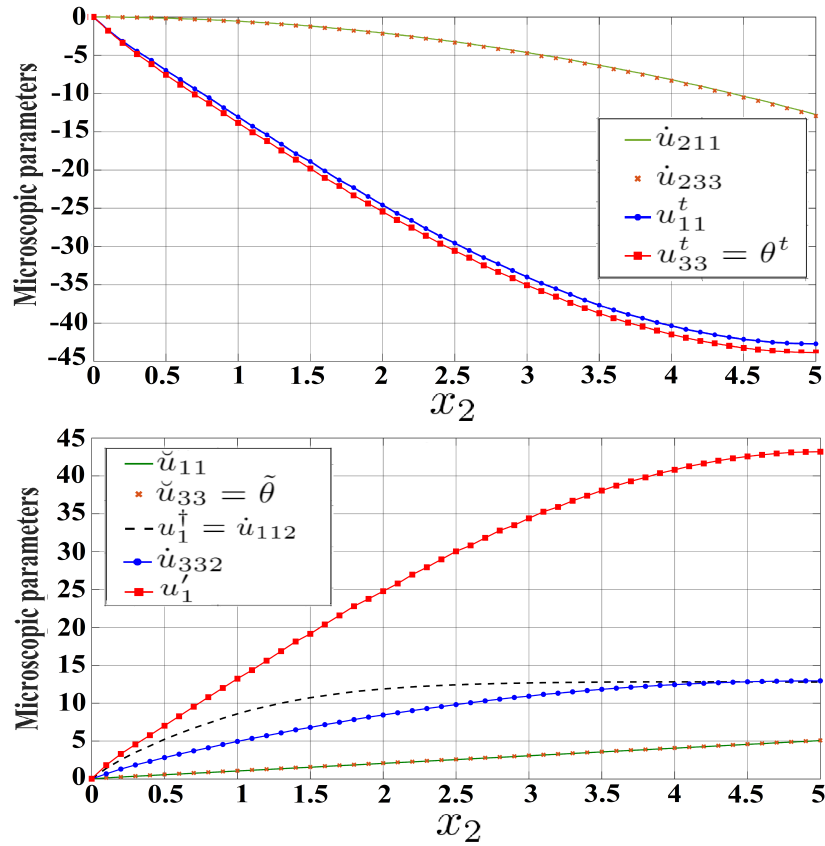
Figure 3: Behavior of the parameters of interest along a line in the x_2-direction which goes through the middle of the rib ($x_1 = 0$ with reference to Figure 2). The displayed numerical results are for the case $e/\ell = 0.25$ and $y_\infty = 5$.

The behaviors of the parameters of interest, those which contribute to the effective boundary conditions, are presented in Figure 3, separating them into

two groups according to their gradients in the x_2-direction (either positive or negative). At the matching interface ($x_2 = y_\infty = 5$), the variables contributing to the effective boundary conditions are independent of x_1 and take the following uniform values:

$$\breve{u}_{11} = 5.0396, \qquad \breve{u}_{33} = \tilde{\theta} = 5.0861,$$

$$u_{11}^\dagger = \dot{u}_{112} = -\dot{u}_{211} = 12.6843, \qquad \dot{u}_{332} = -\dot{u}_{233} = 12.9402,$$

$$u_1' = 43.0376, \qquad u_{11}^t = -42.4485, \qquad u_{33}^t = \theta^t = -43.8582.$$

4.2. Effects of varying the matching interface location

The effect of changing the matching surface distance, y_∞, on the values of the seven independent groups of effective parameters has been analyzed with the aid of successive numerical simulations, varying y_∞ from 2 to 6, as listed in Table 1.

Table 1: Microscopic results found at different values of y_∞ for square ribs with $e/\ell = 0.25$.

y_∞	$\breve{u}_{11}$	$\breve{u}_{33} = \tilde{\theta}$	$u_1^\dagger = \dot{u}_{112} = -\dot{u}_{211}$	$\dot{u}_{332} = -\dot{u}_{233}$	u_1'	u_{11}^t	$u_{33}^t = \theta^t$
2	2.0398	2.0861	2.0819	2.1818	2.8935	-2.8114	-3.0271
3	3.0399	3.0861	4.5575	4.7680	9.5340	-9.2334	-9.7986
4	4.0396	4.0861	8.0795	8.3541	21.8505	-21.5067	-22.7422
5	5.0396	5.0861	12.6843	12.9402	43.0376	-42.4485	-43.8582
6	6.0398	6.0861	18.3994	18.5264	74.2034	-72.2463	-75.1465
	Category (L)		Category (Q)		Category (C)		
	Linear relations		Quadratic relations		Cubic relations		

An in-depth look into the table reveals that we have three categories of relations between the values of the microscopic parameters at the matching interface versus the location of the interface itself; specifically, linear, quadratic, and cubic relations. Fitting the results, we get the following expressions for the closure variables evaluated at y_∞:

$$\breve{u}_{11} = y_\infty + \lambda_x, \qquad \breve{u}_{33} = \tilde{\theta} = y_\infty + \lambda_z,$$

17

$$u_1^\dagger = \dot{u}_{112} = -\dot{u}_{211} = \frac{y_\infty^2}{2} + \lambda_x y_\infty + m_{12}, \quad \dot{u}_{332} = -\dot{u}_{233} = \frac{y_\infty^2}{2} + \lambda_z y_\infty + m_{32},$$

$$u_1' = 2\left[\frac{y_\infty^3}{6} + m_{32}\, y_\infty^2 + \lambda_x\, y_\infty\right] + \mathcal{B},$$

$$u_{11}^t = -2\left[\frac{y_\infty^3}{6} + m_{12}\, y_\infty^2 + \lambda_x\, y_\infty\right] + \mathcal{B}_{1t},$$

$$u_{33}^t = \theta^t = -2\left[\frac{y_\infty^3}{6} + \lambda_z\, \frac{y_\infty^2}{2} + m_{32}\, y_\infty\right] + \mathcal{B}_{3t}.$$

The dimensionless Navier-slip coefficients (λ_x, λ_z), surface permeability coefficients (m_{12}, m_{32}), velocity-flux sensitivity $(\mathcal{B})$, and time-fluctuations coefficients $(\mathcal{B}_{1t}, \mathcal{B}_{3t})$ are only dependent of the geometric parameters of the ribbed surface, e/ℓ in the case of square ribs. These coefficients can be calculated for any geometry of transverse ribs, once the microscopic numerical simulations are conducted with any suitable value of y_∞, and the results of the microscopic parameters at the matching interface are substituted in the fitting equations.

Simpler, accurate methods for the estimation of the coefficients of interest are proposed within the present framework. The Navier-slip coefficients can be calculated by running the simulations of the leading-order systems, forced by S^{12} and S^{32}, with a suitable value of y_∞ to get, respectively, the fields of $\breve{u}_{11}$ and $\breve{u}_{33}$; thereafter, the values of λ_x and λ_z can be found by averaging the corresponding field at the plane $x_2 = 0$. It is interesting that the same fields can then be employed to estimate the values of m_{12} and m_{32}, making use of the numerical result pointed out by Bottaro and Naqvi [7], i.e.:

$$u_1^\dagger = \dot{u}_{112} = -\dot{u}_{211} = \int_{S_{\text{cell}}} \breve{u}_{11}\, \mathrm{d}x_1\, \mathrm{d}x_2,$$

$$\dot{u}_{332} = -\dot{u}_{233} = \int_{S_{\text{cell}}} \breve{u}_{33}\, \mathrm{d}x_1\, \mathrm{d}x_2,$$

with S_{cell} the surface of the representative near-wall cell.

The following values of the coefficients eventually arise when $e/\ell = 0.25$:

$$\lambda_x = 0.03975, \quad \lambda_z = 0.08609, \quad m_{12} = 0.002332, \quad m_{32} = 0.009551,$$

$$\mathcal{B} = 0.0002399, \quad \mathcal{B}_{1t} = -0.0000839, \quad \mathcal{B}_{3t} = -0.0007794.$$

180 *4.3. The formal expressions of the effective boundary conditions*

The expressions of the microscopic dimensionless velocity components are now available up to $\mathcal{O}(\epsilon^1)$, while the microscopic dimensionless temperature (θ) is known up to $\mathcal{O}(\epsilon^2)$. The values of the preceding quantities can be linked to the corresponding dimensionless macroscopic parameters at the matching interface,

185 based on the concept of continuity of velocity (Eq. (4-a)) and temperature (Eq. (4-b)). In particular, it is convenient to obtain the conditions on the outer rim of the ribs, which amounts to specifying $x_2 = 0$ in the matching relations (Eqs. (4-a, b)), along with setting $y_\infty = 0$ in the fitting expressions, given in Section 4.2, for the microscopic parameters contributing to the effective

190 boundary conditions. Finally, we obtain:

$$
\begin{aligned}
U_1\big|_{X_2=0} = {}& \epsilon \left[\lambda_x\, S^{12} + m_{12}\, \mathcal{R}_G \right]_{X_2=0} \\
& + \epsilon^2 \left[m_{12} \frac{\partial S^{22}}{\partial X_1} + \mathcal{B}\,\mathcal{R}_G \frac{\partial \Theta}{\partial X_2} + \mathcal{B}_{1t}\mathcal{R}_G \frac{\partial S^{12}}{\partial t} \right]_{X_2=0} + \mathcal{O}(\epsilon^3), \quad \text{(16-a)}
\end{aligned}
$$

$$
U_2\big|_{X_2=0} = -\epsilon^2 \left[m_{12} \frac{\partial S^{12}}{\partial X_1} + m_{32} \frac{\partial S^{32}}{\partial X_3} \right]_{X_2=0} + \mathcal{O}(\epsilon^3), \quad \text{(16-b)}
$$

$$
U_3\big|_{X_2=0} = \epsilon\, \lambda_z\, S^{32}\big|_{X_2=0} + \epsilon^2 \left[m_{32} \frac{\partial S^{22}}{\partial X_3} + \mathcal{B}_{3t}\mathcal{R}_G \frac{\partial S^{32}}{\partial t} \right]_{X_2=0} + \mathcal{O}(\epsilon^3),
$$

(16-c)

$$
\Theta\big|_{X_2=0} = 1 + \epsilon\, \lambda_z \frac{\partial \Theta}{\partial X_2}\bigg|_{X_2=0} + \epsilon^2\, \mathcal{B}_{3t}\, \mathcal{R}_G\, Pr \frac{\partial^2 \Theta}{\partial X_2\, \partial t}\bigg|_{X_2=0} + \mathcal{O}(\epsilon^3). \quad \text{(16-d)}
$$

The no-slip conditions of the smooth surface are identically retrieved at $\mathcal{O}(\epsilon^0)$. The effective conditions for velocity are similar to those given by Lācis et al. [6] and Bottaro and Naqvi [7] for flow over rough surfaces without heat transfer. Nevertheless, the presence of the buoyancy terms, proportional to $\mathcal{R}_G$

19

and $\mathcal{R}_G \frac{\partial \Theta}{\partial X_2}$ in the equation of the velocity component U_1, and of the time fluctuation terms in the equations of (U_1, U_3, Θ) should be highlighted. We emphasize that the presence of the buoyancy-related term is a first-order contribution to the effective condition for the streamwise velocity, $\hat{U}_1$, and is directly attributed to the assumption that the Grashof number is sufficiently large, i.e. $\epsilon \mathcal{R}_G = \epsilon^2 \sqrt{Gr}$ is of $\mathcal{O}(\epsilon^1)$, and not $\mathcal{O}(\epsilon^2)$.

In dimensional terms, the conditions on the plane $\hat{x}_2 = 0$ read

$$\hat{u}_1\big|_{\hat{x}_2=0} \approx \underbrace{\hat{\lambda}_x \left[\frac{\partial \hat{u}_1}{\partial \hat{x}_2} + \frac{\partial \hat{u}_2}{\partial \hat{x}_1}\right]_{\hat{x}_2=0} + \hat{m}_{12}\frac{\beta\, g\,(\hat{T}_w - \hat{T}_\infty)}{\nu}}_{First-order}$$

$$+ \underbrace{\hat{m}_{12}\left[\frac{\partial}{\partial \hat{x}_1}\left(-\frac{(\hat{p}-\hat{p}_\infty)}{\mu} + 2\frac{\partial \hat{u}_2}{\partial \hat{x}_2}\right)\right]_{\hat{x}_2=0} + \hat{\mathcal{B}}\frac{g\beta}{\nu}\frac{\partial \hat{T}}{\partial \hat{x}_2}\bigg|_{\hat{x}_2=0}}_{Second-order}$$

$$+ \underbrace{\hat{\mathcal{B}}_{1t}\frac{1}{\nu}\frac{\partial}{\partial \hat{t}}\left[\frac{\partial \hat{u}_1}{\partial \hat{x}_2} + \frac{\partial \hat{u}_2}{\partial \hat{x}_1}\right]_{\hat{x}_2=0}}_{Second-order}, \tag{17-a}$$

$$\hat{u}_2\big|_{\hat{x}_2=0} \approx \underbrace{-\hat{m}_{12}\frac{\partial}{\partial \hat{x}_1}\left[\frac{\partial \hat{u}_1}{\partial \hat{x}_2} + \frac{\partial \hat{u}_2}{\partial \hat{x}_1}\right]_{\hat{x}_2=0} - \hat{m}_{32}\frac{\partial}{\partial \hat{x}_3}\left[\frac{\partial \hat{u}_3}{\partial \hat{x}_2} + \frac{\partial \hat{u}_2}{\partial \hat{x}_3}\right]_{\hat{x}_2=0}}_{Second-order}, \tag{17-b}$$

$$\hat{u}_3\big|_{\hat{x}_2=0} \approx \underbrace{\hat{\lambda}_z \left[\frac{\partial \hat{u}_3}{\partial \hat{x}_2} + \frac{\partial \hat{u}_2}{\partial \hat{x}_3}\right]_{\hat{x}_2=0}}_{First-order} + \underbrace{\hat{m}_{32}\frac{\partial}{\partial \hat{x}_3}\left[-\frac{(\hat{p}-\hat{p}_\infty)}{\mu} + 2\frac{\partial \hat{u}_2}{\partial \hat{x}_2}\right]_{\hat{x}_2=0}}_{Second-order}$$

$$+ \underbrace{\hat{\mathcal{B}}_{3t}\frac{1}{\nu}\frac{\partial}{\partial \hat{t}}\left[\frac{\partial \hat{u}_3}{\partial \hat{x}_2} + \frac{\partial \hat{u}_2}{\partial \hat{x}_3}\right]_{\hat{x}_2=0}}_{Second-order}, \tag{17-c}$$

$$\hat{T}\big|_{\hat{x}_2=0} \approx \underbrace{\hat{T}_w}_{Zero-order} + \underbrace{\hat{\lambda}_z \frac{\partial \hat{T}}{\partial \hat{x}_2}\bigg|_{\hat{x}_2=0}}_{First-order} + \underbrace{\hat{\mathcal{B}}_{3t}\frac{1}{\alpha}\frac{\partial^2 \hat{T}}{\partial \hat{x}_2\,\partial \hat{t}}\bigg|_{\hat{x}_2=0}}_{Second-order}. \tag{17-d}$$

The dimensional groups of coefficients $(\hat{\lambda}_x,\ \hat{\lambda}_z)$, $(\hat{m}_{12},\ \hat{m}_{32})$ and $(\hat{\mathcal{B}},\ \hat{\mathcal{B}}_{1t},\ \hat{\mathcal{B}}_{3t})$ are homogeneous to, respectively, a length, a surface area and a volume, and correspond to the product of their dimensionless counterparts times, respectively, l, l^2 and l^3.

21

5. The role of rib height to pitch distance ratio: parametric study

From a practical point of view, it is advantageous to generate a database of the values of the seven dimensionless, geometry-dependent coefficients of interest, to cover a wide range of rib height to pitch distance ratios, e/l, in order to
₂₁₀ enable the direct use of the effective boundary conditions for the macroscopic problems. In this study, the ratio was varied within the range $0.025 \leq e/l \leq 0.8$. For each value of e/l, the procedure described in Sect. 4.2 for the accurate estimation of the coefficients was followed. The resulting database is presented in tabular form (Table 2) and graphically in Figure 4. It is clear that all model
₂₁₅ coefficients peak, in magnitude, within the range $e/\ell = 0.1$ to 0.3, which implies significant velocity and thermal slip. All coefficients tend to zero as e tends to zero or approaches ℓ, for the effective boundary conditions at $x_2 = 0$ to become no-slip and isothermal wall.

Table 2: The upscaled coefficients of interest for different rib height to pitch distance ratios.

e/l	λ_x	λ_z	m_{12}	m_{32}	$\mathcal{B}$	$\mathcal{B}_{1t}$	$\mathcal{B}_{3t}$
0.025	0.02158	0.02296	0.000265	0.000286	0.0000041	-0.0000041	-0.0000046
0.050	0.03667	0.04215	0.000874	0.001037	0.0000270	-0.0000250	-0.0000320
0.075	0.04593	0.05757	0.001601	0.002120	0.0000710	-0.0000580	-0.0000920
0.100	0.05061	0.06949	0.002250	0.003384	0.0001280	-0.0000940	-0.0001850
0.125	0.05188	0.07822	0.002725	0.004716	0.0001855	-0.0001195	-0.0003000
0.150	0.05094	0.08400	0.002979	0.005999	0.0002290	-0.0001297	-0.0004237
0.175	0.04853	0.08738	0.003029	0.007184	0.0002550	-0.0001264	-0.0005449
0.200	0.04567	0.08859	0.002898	0.008188	0.0002651	-0.0001144	-0.0006477
0.225	0.04265	0.08803	0.002663	0.008976	0.0002578	-0.0000992	-0.0007269
0.250	0.03975	0.08609	0.002332	0.009551	0.0002399	-0.0000839	-0.0007794
0.275	0.03699	0.08302	0.002022	0.009892	0.0002171	-0.0000697	-0.0007982
0.300	0.03459	0.07921	0.001718	0.009987	0.0001912	-0.0000593	-0.0007870
0.350	0.03011	0.07011	0.001188	0.009600	0.0001430	-0.0000442	-0.0007011
0.400	0.02589	0.06023	0.000836	0.008612	0.0001024	-0.0000323	-0.0005671
0.500	0.01776	0.04155	0.000434	0.005803	0.0000417	-0.0000136	-0.0002944
0.600	0.01146	0.02624	0.000230	0.003128	0.0000132	-0.0000055	-0.0001188
0.700	0.00662	0.01453	0.000101	0.001326	0.0000041	-0.0000017	-0.0000364
0.800	0.00315	0.00642	0.000031	0.000391	0.0000009	-0.0000004	-0.0000072
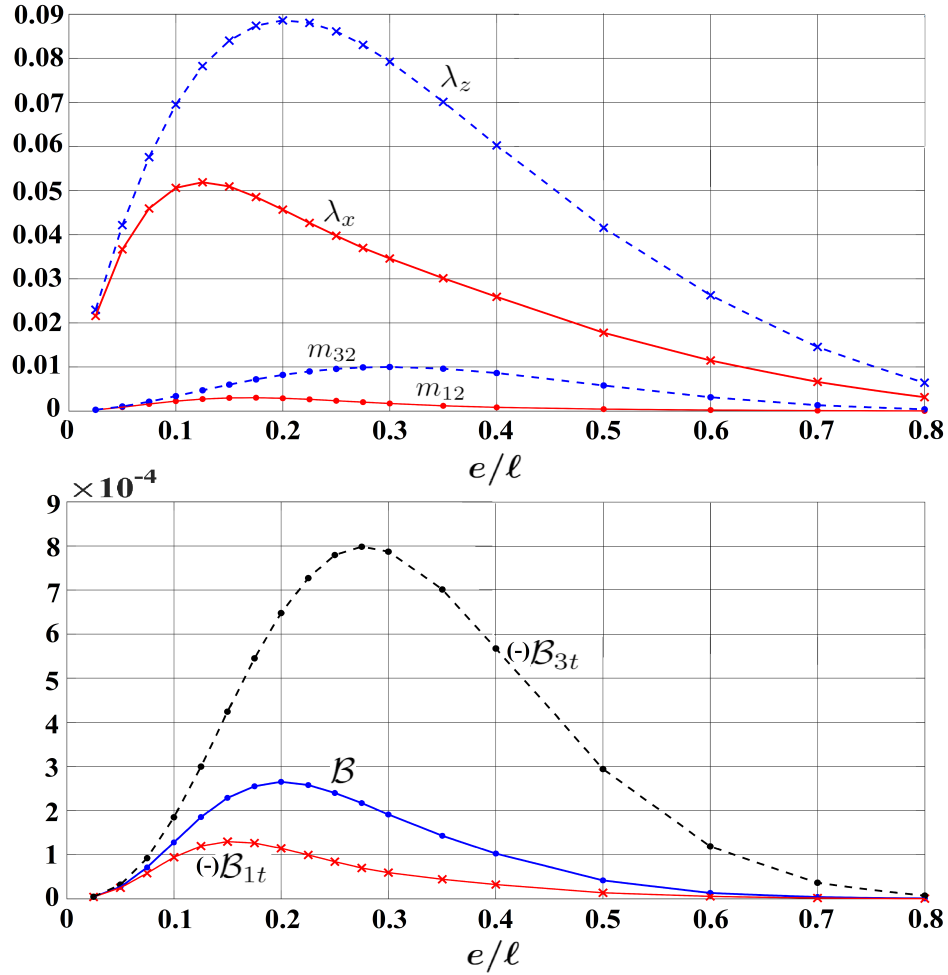
Figure 4: The behavior of the upscaled coefficients of interest with the change of rib height to pitch distance ratio. The curves are fitted on the basis of kriging interpolation.

6. Conclusions

A homogenization-based model for the study of the heat transfer by free convection over regularly microstructured vertical surfaces is proposed. The approach provides a computationally cheap alternative to the standard feature-resolving simulations in the cases where the macroscopic behavior of the flow is of interest, and it has been adopted in the past for the case of rough, microstructured surfaces, in the absence of thermal effects. The procedure, even-

23

tually, yields parameters needed to enforce equivalent velocity and temperature boundary conditions at a plane virtual surface, up to second order in terms of a small parameter $\epsilon = \frac{pattern\ periodicity\ (\ell)}{plate\ length\ (L)}$. Thus, the effective boundary conditions derived here do not contain any empirical parameter.

230

The model is then applied to the case of two-dimensional square ribs characterized by a rib size to pitch distance ratio of 0.25 as a representative example. The auxiliary systems are then reduced to either two-dimensional Stokes-like problems or Laplace-like or Poisson-like problems, which either admit trivial
235 solutions or require a numerical solution in a periodic representative cell of the microscopic domain. The parameters contributing to the effective conditions belong to seven independent groups, i.e. the numerical solution of only seven auxiliary problems is sufficient to completely retrieve the effective conditions. The results are then extrapolated from distant matching surfaces to the plane
240 passing through the outer edges of the ribs, beyond which the macroscopic simulation is intended to be performed. The most significant finding of the procedure is the proposed form of the effective boundary conditions. For the streamwise slip velocity, a buoyancy-representative term acts as a corrector to the classical Navier-slip condition at first order, while pressure-gradient, temperature-
245 gradient, and time-derivative terms appear at second order. A Robin boundary condition appears for the temperature effective condition, where a normal temperature gradient term, with a coefficient identical to Navier's spanwise slip coefficient, corrects the uniform wall temperature. The spanwise slip velocity and the transpiration velocity are also considered, to allow for example using the
250 model in turbulent flow cases where the spanwise and the normal velocity fluctuations are to be resolved in direct or large-eddy numerical simulations [6, 14]. Finally, a parametric study is conducted to investigate the effect of varying the rib size to pitch distance ratio on the values of the coefficients.

255 The proposed approach represents an improvement to the upscaling model of Introïni et al. [19], because: (i) the buoyancy effect is considered in the

24

microscale problem, relaxing the validity restrictions of Introïni's model; consequently, the proposed model yields accurate macroscopic results at relatively high Rayleigh numbers [22]; (ii) the asymptotic homogenization method adopted

₂₆₀ here represents a rigorous tool to formally advance in the order of accuracy; (iii) second-order accurate boundary conditions are attained, an enhancement to the validity range of Introïni's first-order approach; (iv) the inclusion of the transpiration velocity fluctuations allows for turbulent flow simulations at a fraction of the cost of feature-resolving simulations [6, 14].

₂₆₅

Acknowledgements

25

Appendix 1: Auxiliary systems for the problem at order ϵ

The microscopic auxiliary systems at this order are arranged, according to the macroscopic forcing term, in the following groups:

Group (I): Forcing by the gradient of the outer stress (9 systems) $\dfrac{\partial S^{k2}}{\partial X_j}$

$$\frac{\partial \dot{u}_{ijk}}{\partial x_i} = -\breve{u}_{jk}, \qquad \frac{\partial^2 \dot{u}_{ijk}}{\partial x_\ell^2} - \frac{\partial \dot{p}_{jk}}{\partial x_i} = \breve{p}_k \delta_{ij} - 2\frac{\partial \breve{u}_{ik}}{\partial x_j}, \qquad \text{(18-a, b)}$$

subject to

$$\dot{u}_{ijk} = 0 \quad \text{at } x_2 = y_w, \qquad \text{(18-c)}$$

$$-\dot{p}_{jk}\,\delta_{i2} + \left(\frac{\partial \dot{u}_{ijk}}{\partial x_2} + \frac{\partial \dot{u}_{2jk}}{\partial x_i} \right) = -\left(\breve{u}_{ik}\,\delta_{j2} + \breve{u}_{2k}\,\delta_{ij} \right) \quad \text{at } x_2 \to \infty. \qquad \text{(18-d)}$$

Group (II): Forcing by the square of outer stresses (3 systems) $\mathcal{R}_G(S^{k2})^2$

$$\frac{\partial \ddot{u}_{ik}}{\partial x_i} = 0, \qquad \frac{\partial^2 \ddot{u}_{ik}}{\partial x_\ell^2} - \frac{\partial \ddot{p}_k}{\partial x_i} = \breve{u}_{\ell k}\frac{\partial \breve{u}_{ik}}{\partial x_\ell}, \qquad \text{(19-a, b)}$$

subject to

$$\ddot{u}_{ik} = 0 \quad \text{at } x_2 = y_w, \qquad \text{(19-c)}$$

$$-\ddot{p}_k\,\delta_{i2} + \left(\frac{\partial \ddot{u}_{ik}}{\partial x_2} + \frac{\partial \ddot{u}_{2k}}{\partial x_i} \right) = 0 \quad \text{at } x_2 \to \infty. \qquad \text{(19-d)}$$

Group (III): 3 systems: $\mathcal{R}_G S^{12} S^{22}$, $\mathcal{R}_G S^{12} S^{32}$, $\mathcal{R}_G S^{22} S^{32}$
(a) $\mathcal{R}_G S^{12} S^{22}$

$$\frac{\partial \ddot{u}_{i12}}{\partial x_i} = 0, \qquad \frac{\partial^2 \ddot{u}_{i12}}{\partial x_\ell^2} - \frac{\partial \ddot{p}_{12}}{\partial x_i} = \breve{u}_{\ell 1}\frac{\partial \breve{u}_{i2}}{\partial x_\ell} + \breve{u}_{\ell 2}\frac{\partial \breve{u}_{i1}}{\partial x_\ell}, \qquad \text{(20-a, b)}$$

subject to

$$\ddot{u}_{i12} = 0 \quad \text{at } x_2 = y_w, \qquad \text{(20-c)}$$

$$-\ddot{p}_{12}\,\delta_{i2} + \left(\frac{\partial \ddot{u}_{i12}}{\partial x_2} + \frac{\partial \ddot{u}_{212}}{\partial x_i} \right) = 0 \quad \text{at } x_2 \to \infty. \qquad \text{(20-d)}$$

(b) $\mathcal{R}_G S^{12} S^{32}$

$$\frac{\partial \ddot{u}_{i13}}{\partial x_i} = 0, \qquad \frac{\partial^2 \ddot{u}_{i13}}{\partial x_\ell^2} - \frac{\partial \ddot{p}_{13}}{\partial x_i} = \breve{u}_{\ell 1}\frac{\partial \breve{u}_{i3}}{\partial x_\ell} + \breve{u}_{\ell 3}\frac{\partial \breve{u}_{i1}}{\partial x_\ell}, \qquad \text{(21-a, b)}$$

subject to

$$\ddot{u}_{i13} = 0 \qquad \text{at } x_2 = y_w, \qquad \text{(21-c)}$$

$$-\ddot{p}_{13}\,\delta_{i2} + \left(\frac{\partial \ddot{u}_{i13}}{\partial x_2} + \frac{\partial \ddot{u}_{213}}{\partial x_i}\right) = 0 \qquad \text{at } x_2 \to \infty. \qquad \text{(21-d)}$$

(c) $\mathcal{R}_G S^{22} S^{32}$

$$\frac{\partial \ddot{u}_{i23}}{\partial x_i} = 0, \qquad \frac{\partial^2 \ddot{u}_{i23}}{\partial x_\ell^2} - \frac{\partial \ddot{p}_{23}}{\partial x_i} = \breve{u}_{\ell 2}\frac{\partial \breve{u}_{i3}}{\partial x_\ell} + \breve{u}_{\ell 3}\frac{\partial \breve{u}_{i2}}{\partial x_\ell}, \qquad \text{(22-a, b)}$$

subject to

$$\ddot{u}_{i23} = 0 \qquad \text{at } x_2 = y_w, \qquad \text{(22-c)}$$

$$-\ddot{p}_{23}\,\delta_{i2} + \left(\frac{\partial \ddot{u}_{i23}}{\partial x_2} + \frac{\partial \ddot{u}_{223}}{\partial x_i}\right) = 0 \qquad \text{at } x_2 \to \infty. \qquad \text{(22-d)}$$

Group (IV): Coupling through the heat flux (1 system): $\mathcal{R}_G\,\eta$

$$\frac{\partial u_i{}'}{\partial x_i} = 0, \qquad \frac{\partial^2 u_i{}'}{\partial x_\ell^2} - \frac{\partial p'}{\partial x_i} = -\tilde{\theta}\delta_{i1}, \qquad \text{(23-a, b)}$$

subject to

$$u_i{}' = 0 \qquad \text{at } x_2 = y_w, \qquad \text{(23-c)}$$

$$-p'\,\delta_{i2} + \left(\frac{\partial u_i{}'}{\partial x_2} + \frac{\partial u_2{}'}{\partial x_i}\right) = 0 \qquad \text{at } x_2 \to \infty. \qquad \text{(23-d)}$$

Group (V): Forcing by the outer stress (3 systems): $\mathcal{R}_G^2 S^{k2}$

$$\frac{\partial \overline{u}_{ik}}{\partial x_i} = 0, \qquad \frac{\partial^2 \overline{u}_{ik}}{\partial x_\ell^2} - \frac{\partial \overline{p}_k}{\partial x_i} = \breve{u}_{\ell k}\frac{\partial u_i^{\dagger}}{\partial x_\ell} + u_\ell^{\dagger}\frac{\partial \breve{u}_{ik}}{\partial x_\ell}, \qquad \text{(24-a, b)}$$

subject to

$$\overline{u}_{ik} = 0 \qquad \text{at } x_2 = y_w, \qquad \text{(24-c)}$$

$$-\overline{p}_k\,\delta_{i2} + \left(\frac{\partial \overline{u}_{ik}}{\partial x_2} + \frac{\partial \overline{u}_{2k}}{\partial x_i}\right) = 0 \qquad \text{at } x_2 \to \infty. \qquad \text{(24-d)}$$

Group (VI): Forcing by a constant, buoyancy-related term (1 system): $\mathcal{R}_G^3$

$$\frac{\partial u_i^{\ddagger}}{\partial x_i} = 0, \qquad \frac{\partial^2 u_i^{\ddagger}}{\partial x_\ell^2} - \frac{\partial p^{\ddagger}}{\partial x_i} = u_\ell^{\dagger} \frac{\partial u_i^{\dagger}}{\partial x_\ell}, \tag{25-a, b}$$

subject to

$$u_i^{\ddagger} = 0 \quad \text{at } x_2 = y_w, \tag{25-c}$$

$$-p^{\ddagger} \delta_{i2} + \left(\frac{\partial u_i^{\ddagger}}{\partial x_2} + \frac{\partial u_2^{\ddagger}}{\partial x_i} \right) = 0 \quad \text{at } x_2 \to \infty. \tag{25-d}$$

Group (VII): Forcing by outer stress time fluctuation (3 systems): $\mathcal{R}_G \dfrac{\partial S^{k2}}{\partial t}$

$$\frac{\partial u_{ik}^t}{\partial x_i} = 0, \qquad \frac{\partial^2 u_{ik}^t}{\partial x_\ell^2} - \frac{\partial p_k^t}{\partial x_i} = \breve{u}_{ik}, \tag{26-a, b}$$

subject to

$$u_{ik}^t = 0 \quad \text{at } x_2 = y_w, \tag{26-c}$$

$$-p_k^t \delta_{i2} + \left(\frac{\partial u_{ik}^t}{\partial x_2} + \frac{\partial u_{2k}^t}{\partial x_i} \right) = 0 \quad \text{at } x_2 \to \infty. \tag{26-d}$$

Appendix 2: Auxiliary systems for the temperature at order ϵ^2

The eight microscopic auxiliary systems, defining the problem of the order ϵ^2 temperature, are arranged as follows:

Forcing by 2nd derivative of the outer temperature (3 systems): $\dfrac{\partial \eta}{\partial X_k}$

$$\frac{\partial^2 \theta_k^!}{\partial x_i^2} = -2 \frac{\partial \tilde{\theta}}{\partial x_k}, \tag{27-a}$$

subject to

$$\theta_k^! = 0 \quad \text{at } x_2 = y_w, \qquad \frac{\partial \theta_k^!}{\partial x_2} = -\tilde{\theta} \delta_{k2} \quad \text{at } x_2 \to \infty. \tag{27-b, c}$$

Coupling through the outer stress (3 systems): $Pr\mathcal{R}_G \, \eta S^{k2}$

$$\frac{\partial^2 \theta_k^*}{\partial x_i^2} = \breve{u}_{ik} \frac{\partial \tilde{\theta}}{\partial x_i}, \tag{28-a}$$

28

subject to

$$\theta_k^* = 0 \quad \text{at } x_2 = y_w, \qquad \frac{\partial \theta_k^*}{\partial x_2} = 0 \quad \text{at } x_2 \to \infty. \qquad \text{(28-b, c)}$$

Forcing by the outer temperature gradient (1 system): $Pr\mathcal{R}_G^2 \eta$

$$\frac{\partial^2 \theta^{**}}{\partial x_i^2} = u_i^\dagger \frac{\partial \tilde{\theta}}{\partial x_i}, \qquad \text{(29-a)}$$

subject to

$$\theta^{**} = 0 \quad \text{at } x_2 = y_w, \qquad \frac{\partial \theta^{**}}{\partial x_2} = 0 \quad \text{at } x_2 \to \infty. \qquad \text{(29-b, c)}$$

Forcing by time fluctuations of the outer heat flux (1 system): $Pr\mathcal{R}_G \dfrac{\partial \eta}{\partial t}$

$$\frac{\partial^2 \theta^t}{\partial x_i^2} = \tilde{\theta}, \qquad \text{(30-a)}$$

subject to

$$\theta^t = 0 \quad \text{at } x_2 = y_w, \qquad \frac{\partial \theta^t}{\partial x_2} = 0 \quad \text{at } x_2 \to \infty. \qquad \text{(30-b, c)}$$

Appendix 3: Numerical results of $\mathcal{O}(\epsilon^0)$ systems: $e/\ell = 0.25$, $y_\infty = 5$

The systems S^{k2} (Eqs. (6)) represent the forcing of the leading-order problem by the three outer stresses (streamwise, normal, and spanwise). For the sub-system (S^{12}), the results of the Stokes problem ($\breve{u}_{11}$, $\breve{u}_{21}$, $\breve{p}_1$) near the rib are shown in Figure 5. The only result of interest is $\breve{u}_{11}$ which increases monotonically with the coordinate x_2 until reaching a value of 5.0396 at $x_2 = y_\infty = 5$. The result of the decoupled Laplace problem for the sub-system (S^{32}) is shown in Figure 6. The value of $\breve{u}_{33}$ monotonically increases with x_2, reaching the value 5.0861 at the matching surface $x_2 = y_\infty = 5$.
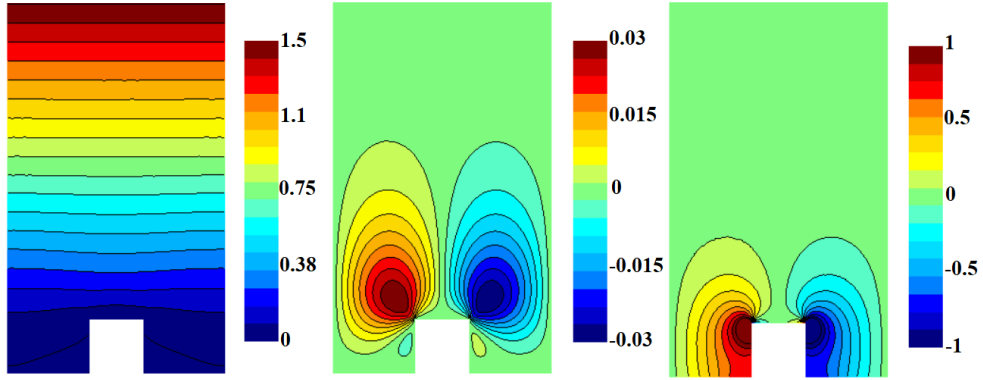
Figure 5: Numerical results in the proximity of the solid surface for: (left) $\breve{u}_{11}$; (center) $\breve{u}_{21}$; (right) $\breve{p}_1$.
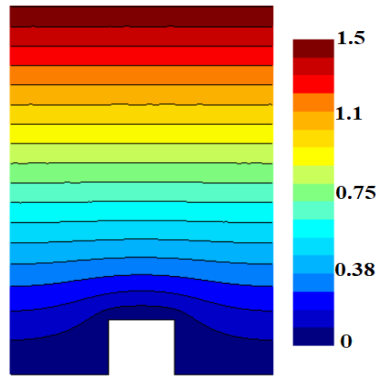
Figure 6: Numerical results for $\breve{u}_{33}$ in the proximity of the solid surface.

The system $\mathcal{R}_G$ (Eqs. (7)) represents the leading-order effect of the buoyancy force on the microscale problem. The results of the Stokes problem $(u_1^\dagger, u_2^\dagger, p^\dagger)$ in the vicinity of the rib are shown in Figure 7. The only result of interest is $u_1^\dagger$ which monotonically increases at a slowing rate with the coordinate x_2, reaching a value of 12.6843 at $x_2 = y_\infty = 5$.

30
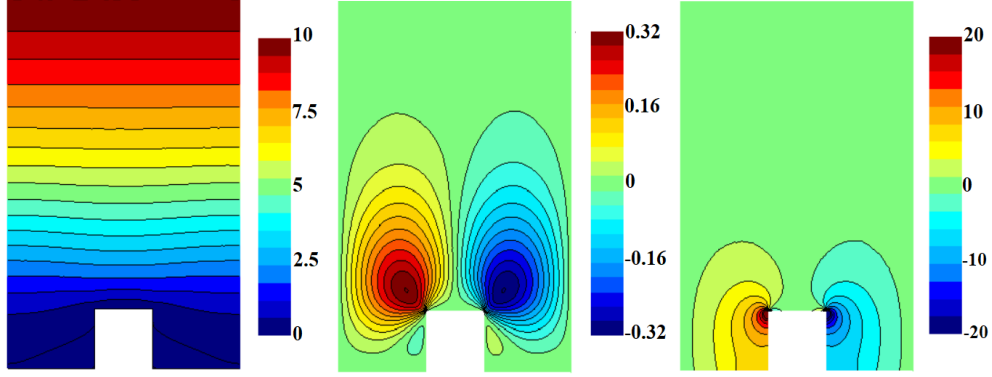
Figure 7: Numerical results in the proximity of the solid surface for: (left) $u_1^\dagger$; (center) $u_2^\dagger$; (right) $p^\dagger$.

Appendix 4: Numerical results of $\mathcal{O}(\epsilon^1)$ systems: $e/\ell = 0.25$, $y_\infty = 5$

For the temperature problem, the similarity between the Laplace system describing the microscopic parameter $\tilde{\theta}$ (Eqs. (11)) and that describing $\breve{u}_{33}$ allows for a solution of $\tilde{\theta}$ identical to that shown in Figure 6. The velocity-related problems may be categorized as follows:

I- Systems with trivial solutions

The similarity between $\tilde{\theta}$ and $\breve{u}_{33}$, in addition to the already mentioned trivial solutions of many parameters in $\mathcal{O}(\epsilon^0)$ problem, simplifies and reduces different systems of equations in $\mathcal{O}(\epsilon^1)$ problem. The systems $\frac{\partial S^{22}}{\partial X_2}$, $\mathcal{R}_G^2 S^{22}$, $\mathcal{R}_G (S^{22})^2$, $\mathcal{R}_G (S^{32})^2$, $\mathcal{R}_G (S^{12} S^{22})$, $\mathcal{R}_G (S^{22} S^{32})$, and $\mathcal{R}_G \frac{\partial S^{22}}{\partial t}$ admit, respectively, the trivial solutions:

$$\frac{\partial S^{22}}{\partial X_2}: \quad \dot{u}_{122} = \dot{u}_{222} = \dot{u}_{322} = 0, \ \dot{p}_{22} = x_2 - y_\infty,$$

$$\mathcal{R}_G^2 S^{22}: \quad \overline{u}_{12} = \overline{u}_{22} = \overline{u}_{32} = \overline{p}_2 = 0,$$

$$\mathcal{R}_G (S^{22})^2: \quad \ddot{u}_{122} = \ddot{u}_{222} = \ddot{u}_{322} = \ddot{p}_{22} = 0,$$

$$\mathcal{R}_G (S^{32})^2: \quad \ddot{u}_{133} = \ddot{u}_{233} = \ddot{u}_{333} = \ddot{p}_{33} = 0,$$

31

$$\mathcal{R}_G(S^{12}S^{22}): \quad \ddot{u}_{112} = \ddot{u}_{212} = \ddot{u}_{312} = \ddot{p}_{12} = 0,$$

$$\mathcal{R}_G(S^{22}S^{32}): \quad \ddot{u}_{123} = \ddot{u}_{223} = \ddot{u}_{323} = \ddot{p}_{23} = 0,$$

$$\mathcal{R}_G\frac{\partial S^{22}}{\partial t}: \quad u_{12}^t = u_{22}^t = u_{32}^t = p_2^t = 0.$$

II- **Systems with all parameters vanishing away from the wall**

Poisson-like systems

300   The systems forced by $\frac{\partial S^{12}}{\partial X_3}$, $\frac{\partial S^{32}}{\partial X_1}$, $\mathcal{R}_G^2 S^{32}$, and $\mathcal{R}_G S^{12}S^{32}$ can be reduced to two-dimensional Poisson-like problems.
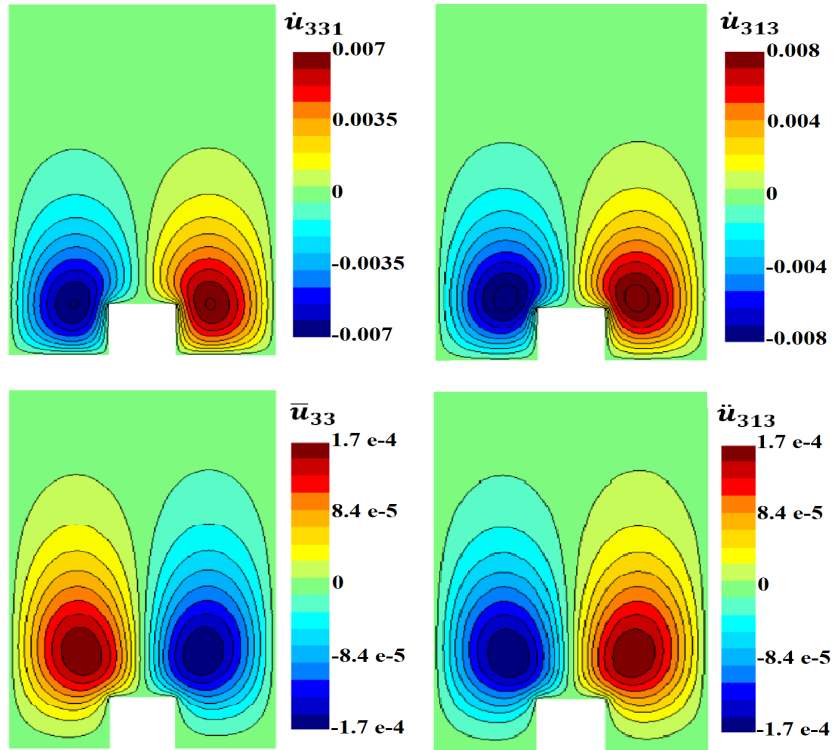
Figure 8: Numerical results of Poisson-like systems, in the $\mathcal{O}(\epsilon^1)$ problem, with no contribution to the effective boundary conditions.

The numerical solutions reveal that the values of the parameters $\dot{u}_{331}$, $\dot{u}_{313}$, $\overline{u}_{33}$,

and $\ddot{u}_{313}$, respectively, vanish away from the ribbed wall, giving no contribution to the effective boundary conditions at the matching surface, as displayed in
305 Figure 8. The other parameters included in the above-mentioned four systems have zero values throughout the unit cell.

Stokes-like systems
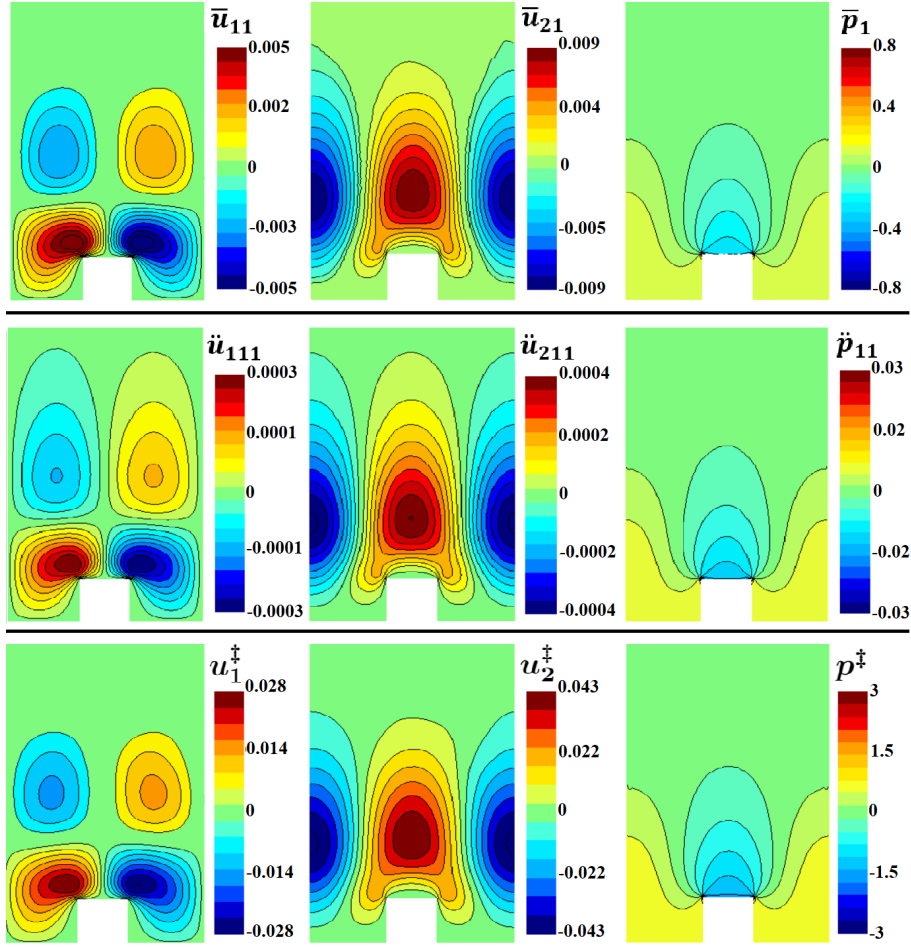
Figure 9: Numerical results of Stokes-like systems, in the $\mathcal{O}(\epsilon^1)$ problem, giving no contribution to the effective boundary conditions: (top) $\mathcal{R}_G^2 S^{12}$ system; (middle) $\mathcal{R}_G(S^{12})^2$ system; (bottom) $\mathcal{R}_G^3$ system.

The systems forced by $\mathcal{R}_G^2 S^{12}$, $\mathcal{R}_G(S^{12})^2$, and $\mathcal{R}_G^3$ can be reduced to two-
310 dimensional Stokes-like problems with the values of $\overline{u}_{31}$, $\ddot{u}_{311}$, and $u_3^{\ddagger}$ equal

33

to zero throughout the unit cell. The non-trivial solutions of the Stokes-like problems show that all included parameters vanish away from the ribbed surface, as can be seen in Figure 9.

III- <u>Systems with non-monotonic behavior along the y-direction</u>

315   The analysis of the systems forced by $\frac{\partial S^{12}}{\partial X_2}$ and $\frac{\partial S^{32}}{\partial X_2}$ shows non-monotonic quadratic behaviors of the parameters $\dot{u}_{121}$ and $\dot{u}_{323}$ along the x_2-direction, with vanishing values at the matching surface, as shown in Figure 10.
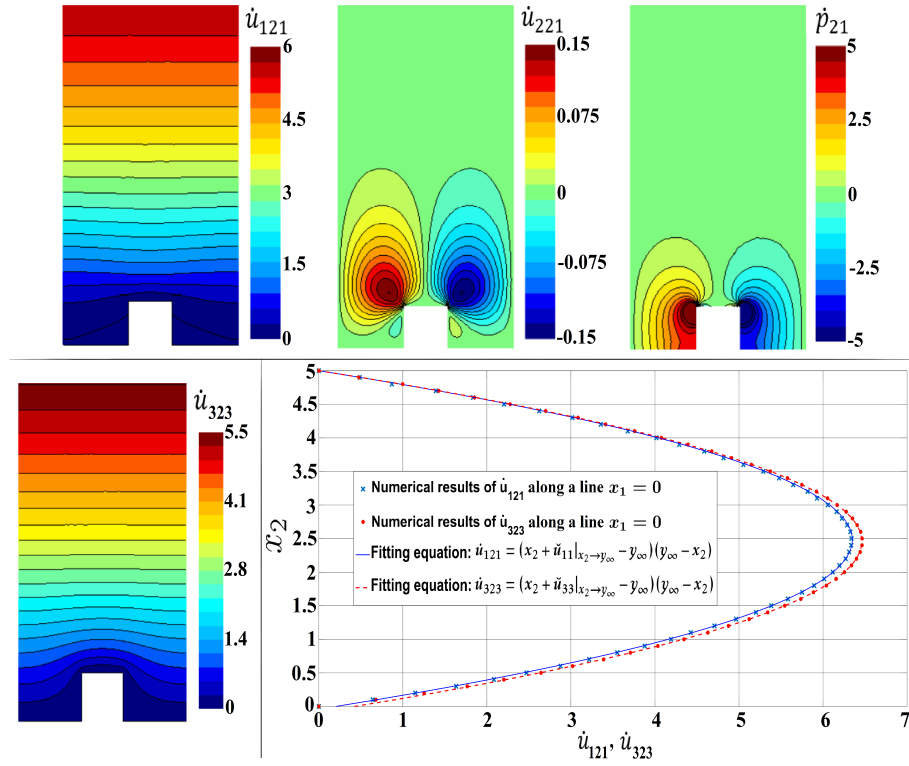
Figure 10: Systems with non-monotonic behavior: (top) $\frac{\partial S^{12}}{\partial X_2}$: the Stokes system; (bottom-left) $\frac{\partial S^{32}}{\partial X_2}$: the Laplace system; (bottom-right) graphical representations of the non-monotonic behaviors, with the quadratic fitting form by Bottaro and Naqvi [7], admissible above $x_2 = 1$.

The other parameters included in the two systems have no contribution to the effective boundary conditions at the matching surface as they either mono-

320   tonically vanish away from the rib ($\dot{u}_{221}$, $\dot{p}_{21}$) or have zero values throughout

34

the whole unit cell ($\dot{u}_{321}$, $\dot{u}_{123}$, $\dot{u}_{223}$, $\dot{p}_{23}$).

IV- Systems with a monotonically-decreasing parameter of interest

Poisson-like system

The system forced by $\mathcal{R}_G \frac{\partial S^{32}}{\partial t}$ can be reduced to a two-dimensional Poisson-like problem in which the only value of interest is u^t_{33}. The contours of u^t_{33} in the vicinity of the rib are shown in Figure 11. The value of this parameter experiences a monotonic decrease along the x_2-direction, reaching a value of about -43.8582 at $x_2 = y_\infty = 5$.
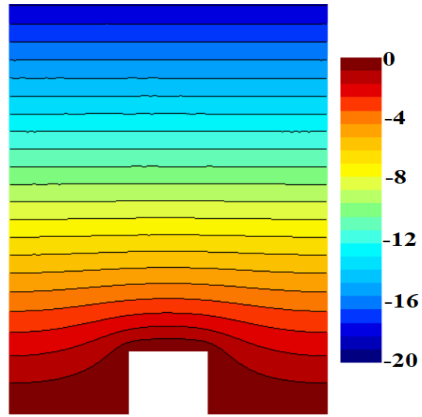
Figure 11: Contours of u^t_{33} in the vicinity of the wall.

Stokes-like systems

The analysis of the systems forced by $\frac{\partial S^{12}}{\partial X_1}$, $\frac{\partial S^{32}}{\partial X_3}$, and $\mathcal{R}_G \frac{\partial S^{12}}{\partial t}$ shows that they become two-dimensional Stokes-like problems with vanishing values of $\dot{u}_{311}$, $\dot{u}_{333}$, and u^t_{31} throughout the unit cell. The numerical results of $\dot{u}_{211}$, $\dot{u}_{233}$, and u^t_{11} show monotonic decrease along x_2, reaching values of about -12.6843, -12.9402, and -42.4485 at the matching interface, respectively. The numerical results of the preceding systems in the vicinity of the rib are shown in Figure 12.
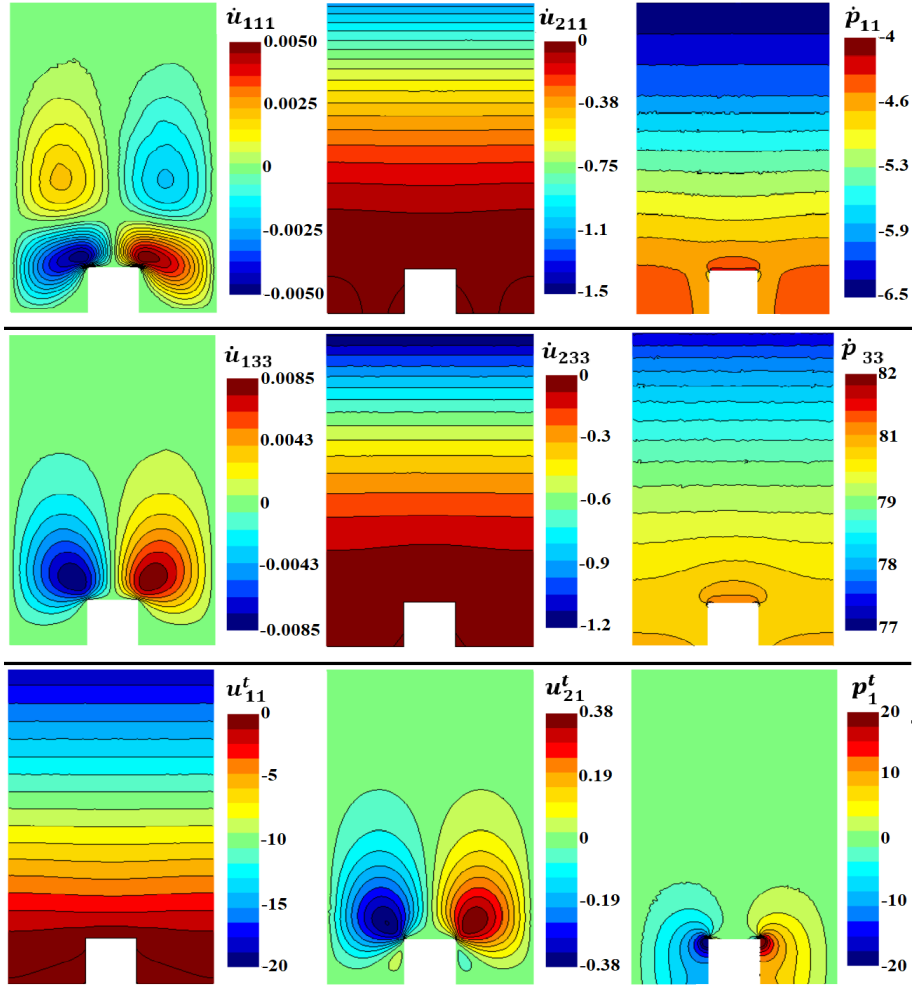
Figure 12: Numerical results of Stokes-like systems, in the $\mathcal{O}(\epsilon^1)$ problem, with parameters having monotonic decrease along the x_2-direction: (top) $\frac{\partial S^{12}}{\partial X_1}$ system; (middle) $\frac{\partial S^{32}}{\partial X_3}$ system; (bottom) $\mathcal{R}_G \frac{\partial S^{12}}{\partial t}$ system.

V- **Systems with a monotonically-increasing parameter of interest**

Poisson-like system

The system forced by $\frac{\partial S^{22}}{\partial X_3}$ can be reduced to two-dimensional Poisson-like problems in which the only value of interest is $\dot{u}_{332}$. The contours of $\dot{u}_{332}$ in the vicinity of the rib are shown in Figure 13. The value of this parameter experiences a monotonic increase with x_2, reaching a value of about 12.9402 at $x_2 = y_\infty = 5$.
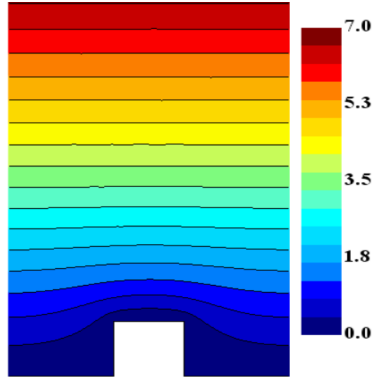
Figure 13: Contours of $\dot{u}_{332}$ in the vicinity of the wall.

Stokes-like systems

The analysis of the systems forced by $\frac{\partial S^{22}}{\partial X_1}$ and $\mathcal{R}_G\eta$ shows that they can be reduced to two-dimensional Stokes-like problems with the values of $\dot{u}_{312}$ and u'_3 equal to zero throughout the unit cell.
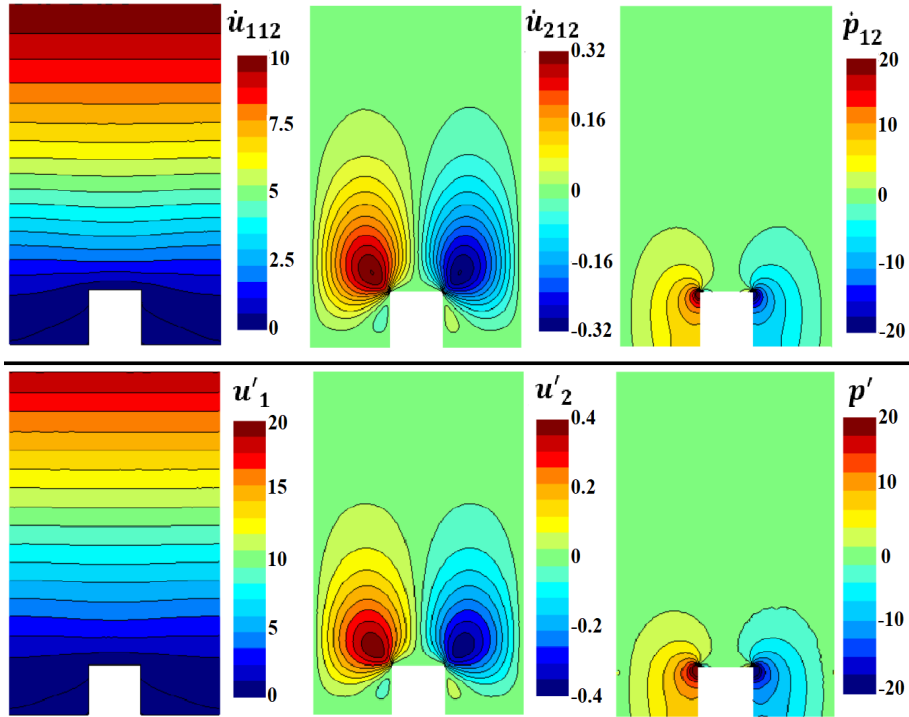
Figure 14: Numerical results of Stokes-like systems, in the $\mathcal{O}(\epsilon^1)$ problem, with parameters having monotonic decrease along the x_2-direction: (top) $\frac{\partial S^{22}}{\partial X_1}$ system; (bottom) $\mathcal{R}_G\eta$ system.

37

The numerical results of $\dot{u}_{112}$ and u_1' show monotonic increase with x_2, reaching

350 values of about 12.6843 and 43.0376 at the matching interface, respectively. The numerical results of the preceding systems in the vicinity of the rib are shown in Figure 14.

Appendix 5: Solution of $\mathcal{O}(\epsilon^2)$ temperature systems: $e/\ell = 0.25$, $y_\infty = 5$

The systems $(R_G\,Pr\,S^{22}\eta)$, $(R_G\,Pr\,S^{32}\eta)$, and $(\frac{\partial \eta}{\partial X_3})$ admit, respectively, the trivial solutions $\theta_2^* = \theta_3^* = \theta_3^! = 0$. For the other systems at this order, similarities are recognized with specific Laplace-like problems in $\mathcal{O}(\epsilon^1)$ problem. In particular, it is simple to see that:

$$\theta_1^! = \dot{u}_{313}, \quad \theta_2^! = \dot{u}_{323}, \quad \theta^{**} = \overline{u}_{33}, \quad \theta^t = u_{33}^t, \quad \theta_1^* = \ddot{u}_{313}.$$

Therefore, the values of these microscopic temperature parameters at $x_2 = y_\infty = 5$ are:

$$\theta_1^! = \theta_2^! = \theta^{**} = \theta_1^* = 0, \quad \theta^t = -43.8582.$$

38

References

[1] I. Babuška, Homogenization and its application. Mathematical and computational problems, in: Numerical Solution of Partial Differential Equations–III, Academic Press, 1976, pp. 89–116. `doi:10.1016/B978-0-12-358503-5.50009-9`.

[2] B. Engquist, P. E. Souganidis, Asymptotic and numerical homogenization, Acta Numerica 17 (2008) 147–190. `doi:10.1017/S0962492906360011`.

[3] S. Jiménez Bolaños, B. Vernescu, Derivation of the Navier slip and slip length for viscous flows over a rough boundary, Physics of Fluids 29 (5) (2017) 057103. `doi:10.1063/1.4982899`.

[4] G. A. Zampogna, J. Magnaudet, A. Bottaro, Generalized slip condition over rough surfaces, Journal of Fluid Mechanics 858 (2019) 407–436. `doi:10.1017/jfm.2018.780`.

[5] C. Navier, Mémoire sur les lois du mouvement des fluides, Mémoires de l'Académie Royale des Sciences de l'Institut de France 6 (1823) 389–440.

[6] U. Lācis, Y. Sudhakar, S. Pasche, S. Bagheri, Transfer of mass and momentum at rough and porous surfaces, Journal of Fluid Mechanics 884 (2020) A21. `doi:10.1017/jfm.2019.897`.

[7] A. Bottaro, S. B. Naqvi, Effective boundary conditions at a rough wall: a high-order homogenization approach, Meccanica 55 (9) (2020) 1781–1800. `doi:10.1007/s11012-020-01205-2`.

[8] K. Kamrin, M. Z. Bazant, H. A. Stone, Effective slip boundary conditions for arbitrary periodic surfaces: the surface mobility tensor, Journal of Fluid Mechanics 658 (2010) 409–437. `doi:10.1017/S0022112010001801`.

[9] P. Luchini, Linearized no-slip boundary conditions at a rough surface, Journal of Fluid Mechanics 737 (2013) 349–367. `doi:10.1017/jfm.2013.574`.

[10] J. Guo, S. Veran-Tissoires, M. Quintard, Effective surface and boundary conditions for heterogeneous surfaces with mixed boundary conditions, Journal of Computational Physics 305 (2016) 942–963. `doi:10.1016/j.jcp.2015.10.050`.

[11] G. A. Zampogna, S. B. Naqvi, J. Magnaudet, A. Bottaro, Compliant riblets: Problem formulation and effective macrostructural properties, Journal of Fluids and Structures 91 (2019) 102708. `doi:10.1016/j.jfluidstructs.2019.10270`.

[12] Y. Sudhakar, U. Lācis, S. Pasche, S. Bagheri, Higher-order homogenized boundary conditions for flows over rough and porous surfaces, Transport in Porous Media 136 (1) (2021) 1–42. `doi:10.1007/s11242-020-01495-w`.

[13] S. B. Naqvi, A. Bottaro, Interfacial conditions between a free-fluid region and a porous medium, International Journal of Multiphase Flow 141 (2021) 103585. `doi:10.1016/j.ijmultiphaseflow.2021.103585`.

[14] A. Bottaro, Flow over natural or engineered surfaces: an adjoint homogenization perspective, Journal of Fluid Mechanics 877 (2019) P1. `doi:10.1017/jfm.2019.607`.

[15] M. Cavazzuti, M. A. Corticelli, Optimization of a buoyancy chimney with a heated ribbed wall, Heat and Mass Transfer 44 (4) (2008) 421–435. `doi:10.1007/s00231-007-0255-6`.

[16] J. Hærvig, H. Sørensen, Natural convective flow and heat transfer on unconfined isothermal zigzag-shaped ribbed vertical surfaces, International Communications in Heat and Mass Transfer 119 (2020) 104982. `doi:10.1016/j.icheatmasstransfer.2020.104982`.

[17] L.-S. Yao, Natural convection along a vertical complex wavy surface, International Journal of Heat and Mass Transfer 49 (1-2) (2006) 281–286. `doi:10.1016/j.ijheatmasstransfer.2005.06.026`.

[18] M. Nishikawa, H. Otomo, Y. Yoshida, J. Deguchi, M. Tsukamoto, T. Yamamoto, The cooling mechanism of minuscule ribbed surfaces, Scientific Reports 10 (1) (2020) 1–6. `doi:10.1038/s41598-020-62288-1`.

[19] C. Introïni, M. Quintard, F. Duval, Effective surface modeling for momentum and heat transfer over rough surfaces: application to a natural convection problem, International Journal of Heat and Mass Transfer 54 (15-16) (2011) 3622–3641. `doi:10.1016/j.ijheatmasstransfer.2011.03.019`.

[20] D. Bechert, M. Bartenwerfer, The viscous flow on surfaces with longitudinal ribs, Journal of Fluid Mechanics 206 (1989) 105–129. `doi:10.1017/S0022112089002247`.

[21] P. Luchini, F. Manzo, A. Pozzi, Resistance of a grooved surface to parallel flow and cross-flow, Journal of Fluid Mechanics 228 (1991) 87–109. `doi:10.1017/S0022112091002641`.

[22] E. N. Ahmed, A. Bottaro, G. Tanda, Natural convection along a micropatterned vertical wall. Part 2: Validation of the macroscopic model for the case of transverse square ribs, International Journal of Heat and Mass Transfer. Submitted (2021).